

## Graphical Abstract

### **Periodic Empirical Operator Framework for Inverse Scattering and Structural Health Monitoring**

R. G. Wueest, J. Mueller, J. Aichele, H. R. Thomsen

## Highlights

### **Periodic Empirical Operator Framework for Inverse Scattering and Structural Health Monitoring**

R. G. Wueest, J. Mueller, J. Aichele, H. R. Thomsen

- Presents a fully vectorized linear operator framework for inverse scattering in NDT.
- Relies solely on the principles of linear time-invariant (LTI) systems, avoiding the need for theoretical assumptions about wave propagation.
- Enforces periodic discrete time, enabling FFT-diagonalizable circular convolution operators which are solvable using the Tikhonov regularized inverse.
- Localizes sub-wavelength sized defects in both simulated aluminum plates and real-world CFRP plates.
- Post-calibration, only sparse sensor measurements are needed for rapid health monitoring.

# Periodic Empirical Operator Framework for Inverse Scattering and Structural Health Monitoring

R. G. Wueest<sup>a,\*1</sup> (Researcher), J. Mueller<sup>b</sup> (Advisor), J. Aichele<sup>b</sup> (Advisor) and H. R. Thomsen<sup>b,2</sup> (Advisor)

<sup>a</sup>Department of Physics, ETH Zürich, 8092, Zürich, Switzerland

<sup>b</sup>Department of Earth Sciences, ETH Zürich, 8092, Zürich, Switzerland

## ARTICLE INFO

### Keywords:

Inverse scattering  
Ultrasonic guided waves  
Laser Doppler vibrometry (LDV)  
Empirical impulse response  
Circular convolution  
Tikhonov regularization  
Structural health monitoring

## ABSTRACT

We present an empirically calibrated, fully vectorized linear-operator framework for inverse scattering, motivated by challenges in non-destructive testing (NDT) and structural health monitoring (SHM) where reliable forward models are difficult to obtain and maintain. The method enables defect localization without requiring an explicit physical model of wave propagation. Source–receiver impulse-response operators are constructed through a one-time calibration using bonded piezoelectric transducers for excitation and dense Laser Doppler Vibrometer (LDV) measurements. Enforcing discrete periodic time behavior represents propagation as circular convolution, yielding circulant operators diagonalizable via the discrete Fourier transform (DFT) and allowing defect localization to be posed as a Tikhonov-regularized linear inverse problem using only sparse monitoring data.

Experimental validation on a bidirectional carbon-fiber-reinforced polymer (CFRP) plate demonstrates sub-wavelength localization of a  $1 \text{ cm}^3$  adhered defect using measurements acquired solely at transducer locations after calibration. Computational cost is concentrated in the calibration stage, while subsequent evaluations reduce to rapid matrix–vector operations. Additional simulations complement the experimental results and probe performance across defect scenarios and sensing configurations, including proof-of-concept localization in a single-transducer (pulse-echo) setting.

Relying only on linear time-invariant system assumptions, the framework provides a data-driven alternative for NDT and SHM in situations where maintaining accurate digital twins is impractical, and may extend to other wave-based sensing applications.

## 1. Introduction

Structural Health Monitoring (SHM) of engineered components seeks to localize and characterize defects before they compromise structural integrity. The relevance of SHM is closely linked to the cost of failure, which is particularly critical in aviation, and has motivated extensive research on monitoring approaches for relatively simple, flat structures [34]. Among the available techniques, piezoelectric transducers are attractive from a commercial perspective because of their low cost and ease of integration. Nevertheless, significant difficulties arise when these concepts are transferred to carbon-fiber reinforced polymers (CFRPs) [19], and a range of dedicated strategies for CFRP inspection have therefore been investigated [14, 31]. Interpreting guided-wave measurements in such materials is inherently complex: overlapping modes often demand dedicated processing, such as ridge-based time–frequency analysis, beamforming, or migration to extract meaningful arrivals [27], while benign geometric features, multiple reflections, and mode conversions at joints and thickness transitions generate coherent clutter that can obscure damage signatures [3, 24]. These effects are amplified by the pronounced anisotropy, laminate heterogeneity, and viscoelastic damping of CFRPs, which lead to direction- and frequency-dependent dispersion and attenuation [2, 25]. Curvature, stiffeners, and adhesive interfaces introduce additional localized scattering, and in large curved assets such as rocket fuselages or wind-turbine blades, spatially varying thickness and fiber orientation challenge travel-time–based concepts [35, 6, 18, 23, 26].

Sparse monitoring of Lamb waves using a limited number of piezoelectric sensors [32] would therefore be highly attractive. However, such approaches generally rely on detailed numerical forward models. Modern numerical frameworks, including finite- and spectral-element solvers combined with higher-order plate formulations have proven capable of reproducing dispersion, mode conversion, and multi-path scattering in anisotropic laminates with high

\* richard.wuest@protonmail.com (R.G. Wueest); thomsenh@ethz.ch (H.R. Thomsen)  
ORCID(s):

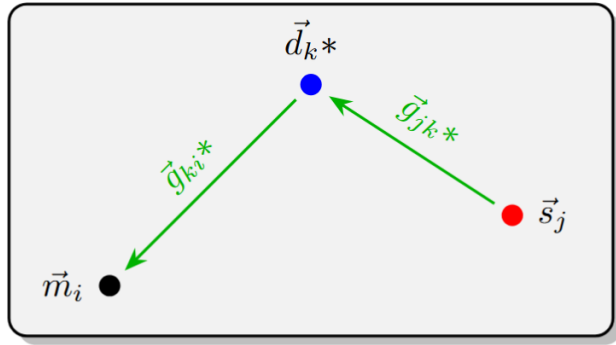


**Figure 1:** Visualization on how a source at location  $j$  propagates to a defect at location  $k$ , which then re-emits the wave. Afterwards, it propagates to a receiver location  $i$ . As an equation, the image visualizes  $\vec{m}_i = \vec{g}_{kj} * \vec{d}_k * \vec{g}_{ik} * \vec{s}_j$ .

fidelity while remaining computationally efficient at ultrasonic frequencies [2, 20]. Nevertheless, such models are difficult to maintain for composite structures [30, 21]. CFRP components, in particular, exhibit variability arising from lay-up and manufacturing processes that undermines the reliability of predictive digital twins [5, 11]. In response to these limitations, data-driven strategies based on Laser Doppler Vibrometry (LDV) have gained increasing attention as a means to capture rich wavefield information directly from the structure and to reduce dependence on uncertain a priori models [7, 28].

This paper validates a novel method based on empirical linear operators[4][17] and a fundamentally periodic time formulation. The result is a matrix based description of the system and it's inversion to solve for defects [1]. We excite the structure with bonded piezoelectric transducers and use an LDV to perform a dense, one-time calibration LDV scan that constructs source–receiver impulse-response operators. Wave propagation is treated on a discrete cyclic time axis so that it acts as circular convolution, diagonalized by the discrete Fourier transform (DFT). By designing the excitation to be strictly periodic and ensuring no other sources act on the object, the cyclic time embedding is valid by construction. We impose time periodic behavior in the setup, and thus the frequency treatment becomes equivalent to the time domain treatment. Within a single-scattering formulation, defect localization is solved via Tikhonov-regularized inverse[29][12] using only sparse monitoring data at the transducer locations. We validate the approach experimentally on an anisotropic CFRP plate, demonstrating sub-wavelength localization from sparse measurements.

## 2. Mathematical framework

Before presenting the experimental results, we first introduce the mathematical framework underlying the proposed defect-detection approach.

### 2.1. System assumptions

We assume: (i) linearity; (ii) time invariance; (iii) reciprocity; (iv) practical flatness (LDV access); and (v) the ability to control the excitation of the material relative to noise.

Assumptions (i), (ii), and (iii) are naturally satisfied for mechanical waves under standard conditions. Assumption (iv) refers to geometries where the object thickness is small relative to its lateral dimensions, typically valid for plate-like components such as aircraft fuselage panels and shell structures. Assumption (v) simply requires a controlled excitation capability, which is standard in active NDT/SHM configurations using piezoelectric or electromagnetic transducers.

### 2.2. Terminology and Notation

We work with discrete-time vectors and matrices throughout. The spatial domain is discretized into a set of points indexed by integers without implying any particular geometric arrangement. For instance, a  $100 \times 100$  scan grid of a square plate yields 10,000 points labeled 1 through 10,000, with the specific mapping arbitrary, but fixed.

When a transducer emits a signal at location  $i$ , represented by time-domain vector  $\vec{s}_i$ , the observed signal  $\vec{m}_j$  at location  $j$  is given by the convolution with the impulse response  $\vec{g}_{ij}$  between those locations:  $\vec{m}_j = \vec{g}_{ij} * \vec{s}_i$ . This formulation separates spatial indices (subscripts) from the time-domain representation (vectors).

For computational implementation, these vectors correspond to discrete-time samples over a fixed acquisition window, with all operations respecting the imposed periodicity described in subsequent sections.

### 2.3. Periodic time and discrete representation

Repeating the excitations enforces periodicity so that the time axis can be treated on a discrete cyclic domain. Any impulse response between locations  $i$  and  $j$  is then a circular-convolution operator  $G_{ij}$ , represented by a circulant (circular Toeplitz) matrix fully determined by its first column (the sampled impulse-response vector  $\vec{g}_{ij}$ ). Explicitly, for  $\vec{g}_{ij} = (g_0, g_1, \dots, g_{n-1})^T$ ,

$$G_{ij} = \begin{pmatrix} g_0 & g_{n-1} & \cdots & g_1 \\ g_1 & g_0 & \cdots & g_2 \\ \vdots & \vdots & \ddots & \vdots \\ g_{n-1} & g_{n-2} & \cdots & g_0 \end{pmatrix} \quad (1)$$

so that  $G_{ij}\vec{v} = \vec{g}_{ij} * \vec{v}$  (circular convolution). All such operators are diagonalized by the discrete Fourier transform (DFT), enabling component-wise multiplication in the frequency domain.

### 2.4. Empirical impulse responses

For a transducer  $s$  and measurement point  $i$  (grid or other transducer), the response is modeled as a circular convolution:

$$\vec{m}_i = G_{is}\vec{s}_s = \vec{g}_{is} * \vec{s}_s \quad (2)$$

where  $G_{is}$  is circulant (first column  $\vec{g}_{is}$ ). Directional (mode) decomposition is intentionally omitted because the LDV records only the scalar out-of-plane velocity at each sampled point.

Both  $\vec{m}_i$  and  $\vec{G}_{is}$  are obtained from measurements. The impulse response of the medium  $\vec{g}_{ij}$  is then calculated as the regularized least squares solution of equation 2 of multiple sets of noisy measurements. The solution can be computed component wise in the frequency domain: Let  $\{\langle \vec{s}_{s,p}, \vec{m}_{i|s,p} \rangle\}_{p=1}^P$  denote  $P$  repeated acquisitions. In the frequency domain (hats denote DFT components), for each frequency bin  $f$  we solve the Tikhonov-regularized least-squares problem in frequency domain:

$$\min_{\hat{g}_{is}(f)} \sum_{p=1}^P \left| \hat{m}_{i|s,p}(f) - \hat{s}_{s,p}(f)\hat{g}_{is}(f) \right|^2 + \alpha |\hat{g}_{is}(f)|^2 \quad (3)$$

with regularization parameter  $\alpha > 0$ . The closed-form solution is:

$$\hat{g}_{is}^{\text{reg}}(f) = \frac{\sum_p \overline{\hat{s}_{s,p}(f)} \hat{m}_{i|s,p}(f)}{\sum_p |\hat{s}_{s,p}(f)|^2 + \alpha} \quad (4)$$

The result is a stabilized impulse-response function that does not rely on assuming specific noise characteristics.  $\alpha$  must just be a small number ( $\approx 10^{-7}$ ) to assert no singularity errors happen. The exact choice does not affect the final solution in any noticeable ways.

The impulse response is called “empirical” in the sense that the source signal  $\vec{s}_s$  is the entire time-domain waveform recorded at the source position. In other words, we do not distinguish between the energy injected by the piezo and the subsequent local reverberations in the measured signal.

### 2.5. Defect model

Since defects also satisfy the assumptions in Section 2.1, their effects can be modeled using circular convolutions. Within the single-scattering (Born-type) approximation, the scattering process is illustrated in Fig. 1. We assume a *delta-like* temporal reflection kernel, so each defect is represented by a scalar amplitude  $d_k$  at its spatial location. Algebraically, this corresponds to selecting only the first canonical temporal basis vector  $\vec{d}_k = \vec{e}_0$ , and physically, it corresponds to a defect position re-emitting the incoming wave immediately. See section C.4 for a generalization of this approach.

## 2.6. Operator assembly

For an emitter at position  $j$  and a measurement at position  $i$ , the measured signal consists of a direct propagation term and first-order (single-scattered) contributions, as illustrated in Fig. 1:

$$\vec{m}_i = \vec{g}_{ij} * \vec{s}_j + \sum_{k=1}^N \vec{g}_{ik} * \vec{d}_k * \vec{g}_{kj} * \vec{s}_j. \quad (5)$$

Here, “single scattering” means first order in *defect-induced* scattering. Boundary reflections and other multipath propagation of the undamaged plate are already embedded in the empirically measured impulse responses  $\vec{g}_{ij}$ ; only terms with multiple defect interactions are neglected.

It can be rewritten in matrix form:

$$\vec{m}_i = G_{ij}\vec{s}_j + \sum_{k=1}^N G_{ik}D_kG_{kj}\vec{s}_j. \quad (6)$$

Using the commutativity of circular convolution, restate the problem as

$$\Delta\vec{m}_{ij} := \vec{m}_i - G_{ij}\vec{s}_j = \sum_{k=1}^N (G_{ik}G_{kj}S_j)\vec{d}_k. \quad (7)$$

Writing the defect vectors  $\vec{d}_k$  as a single vector:

$$\vec{\mathbf{d}}_{\text{full}} := \begin{bmatrix} \vec{d}_1 \\ \vec{d}_2 \\ \vdots \\ \vec{d}_N \end{bmatrix} \quad (8)$$

The problem can be restated as a general matrix problem with

$$L_{ij}^{\text{gen}} := [ G_{i1}G_{1j}S_j \mid G_{i2}G_{2j}S_j \mid \dots \mid G_{iN}G_{Nj}S_j ] \quad (9)$$

so that

$$\Delta\vec{m}_{ij} = L_{ij}^{\text{gen}} \vec{\mathbf{d}}_{\text{full}}. \quad (10)$$

This system is typically highly underdetermined, and even when it is not, it is too large for practical computation. In our use case, the fully time-resolved defect vector would have dimension  $N_{\text{grid}}N_t \approx 10^6$  (with  $N_{\text{grid}}$  spatial grid points and  $N_t$  time samples per period).

However, from the assumption that scatterers generally re-emit waves almost immediately, we can restrict the defect vectors  $\vec{d}_k$  around a small set of temporal basis functions. As mentioned in the previous section, we continue with the simplest case where  $\vec{d}_k = d_k * \vec{e}_0$ , i.e., a 1D basis. Since every defect at any location is parameterized by a single parameter  $d_k$ , the full defect vector can be represented as

$$\vec{\mathbf{d}} := \begin{bmatrix} d_1 \\ d_2 \\ \vdots \\ d_N \end{bmatrix} \quad (11)$$

and integrated into the problem by including the basis vectors into the problem:

$$L_{ij} := [ G_{i1}G_{1j}S_j\vec{e}_0 \mid G_{i2}G_{2j}S_j\vec{e}_0 \mid \dots \mid G_{iN}G_{Nj}S_j\vec{e}_0 ], \quad (12)$$

where  $\vec{e}_0$  in this equation is to be understood as a column vector shaped matrix. The final problem statement for one emitter at  $i$  and sensor at  $j$  is then

$$\Delta \vec{m}_{ij} = L_{ij} \vec{d}. \quad (13)$$

For multiple sensor-emitter pairs, "stacking" the selected  $(i, j)$  pairs yields the global residual system. For example for one emitter at (1) and two sensors at (2,3):

$$\vec{m}_{\text{full}} = \begin{bmatrix} \Delta \vec{m}_{12} \\ \Delta \vec{m}_{13} \end{bmatrix} \quad L_{\text{full}} = \begin{bmatrix} L_{12} \\ L_{13} \end{bmatrix} \quad \vec{m}_{\text{full}} = L_{\text{full}} \vec{d} \quad (14)$$

Which corresponds to a [[1,2][1,3]] system. The general case can be much much larger, as in our cases presented, will be using 5 transducers with 10 total emitter-sensor pairings. (See appendix C.2 for details)

We have reduced the problem statement to the linear system in equation (14). The only approximations made are the discretization of space, the assumption of first-order scattering and immediate reflection property of defects.

## 2.7. Regularized inversion

We solve for  $\vec{d}$  in equation 14. Let  $\mathcal{L} = L_{\text{full}}$  and  $\mathbf{m} = \vec{m}_{\text{full}}$  from equation 14. We solve the linear inverse problem by finding  $\vec{d}$  to minimize following expression:

$$\operatorname{argmin}_{\vec{d}} \|\mathcal{L}\vec{d} - \vec{m}\|_2^2 + \lambda \|\Gamma\vec{d}\|_2^2, \quad (15)$$

where  $\Gamma$  specifies the penalty metric (a weighting / masking matrix) and  $\lambda > 0$  controls the trade-off between data fit and stabilization. The normal equations yield the closed form [15] [13]

$$\vec{d} = (\mathcal{L}^T \mathcal{L} + \lambda \Gamma)^{-1} \mathcal{L}^T \vec{m}. \quad (16)$$

The solution can be computed directly iteratively, or by first computing the matrix  $(\mathcal{L}^T \mathcal{L} + \lambda \Gamma)^{-1} \mathcal{L}^T$  (more expensive), and saving it. Allowing a rapid computation of  $\vec{d}$  though a matrix vector multiplication of many new measurement sets  $\vec{m}$ .

If  $\Gamma$  is the identity matrix, we recover standard Tikhonov regularization, which penalizes the Euclidean norm  $\|\vec{d}\|_2^2$ . In practice, however, real systems can show small changes in pulse shape and amplitude between calibration and monitoring. The inversion would then explain these differences by placing strong "defects" directly at or near the transducer locations, which contaminates the rest of the reconstruction.

To isolate this effect, we choose  $\Gamma$  to be diagonal. Entries corresponding to grid points at the transducers, and in a small neighborhood around them, are set to zero, all other diagonal entries are set to one. Coefficients in these unpenalized regions can adjust to absorb pulse variations without influencing the rest of the defect map. When visualizing the result, these regions are masked out (set to zero), since they mostly reflect pulse corrections rather than physical defects.

The optimal regularization parameter  $\lambda$  in this paper is chosen with no particular method. In the examples of this paper, we are presenting the solution using the optimal parameters as is without discussing it. More formal methods of finding the optimal  $\lambda$  are explored in [16], and the exploration of the effects of different parameter choices for the presented method are documented in [33].

## 3. Experimental Setup

The test specimen is a 26.8 cm  $\times$  26.8  $\times$  0.14 cm bi-directional CFRP plate (8 layers,  $[0^\circ_2/90^\circ_2]_s$ , HexPly 8552/AS4). Five low-cost brass–ceramic piezoelectric discs with a diameter of 12mm were bonded to the plate using a Crystalbond adhesive. As shown in Section 2.4, the method is independent of the source transfer function, and thus works for a wide range of unknown coupling properties.

The actuators were driven via a periodic pulse train with a 2 ms repetition period, using a 80 kHz Ricker wavelet as the pulse shape. A 3D LDV was used to scan the plate on a 104  $\times$  104 square grid, recording the full 3-component velocity vector over time. Figure 3 shows one frame of the measurement. For this work, we use only the out of plane Vz component, which is excited strongest by the piezoelectric sources. The potential use of all three velocity components is discussed in A.1.

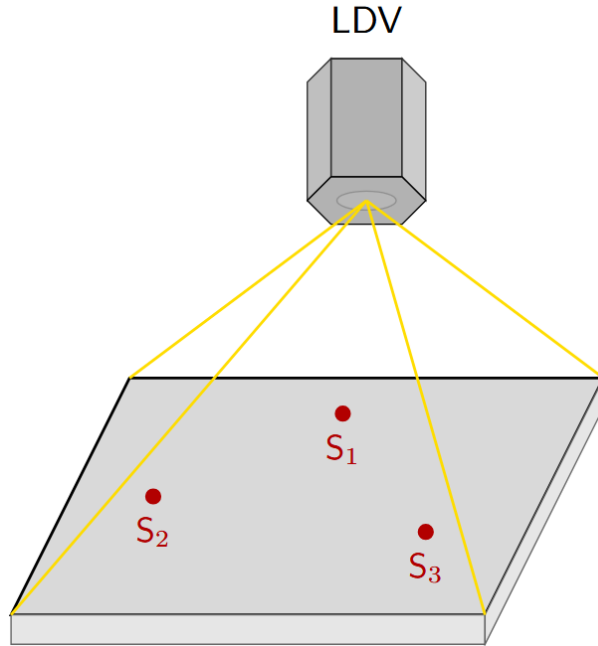


**Figure 2:** TODO: To be replaced with real world setup figs

This scan was repeated for each of the five transducers, which constitute the one-time calibration step. Data were sampled at 625 kHz and low-pass filtered to 50 kHz prior to computation. Each grid location was acquired with 10 repeats 5 separate times. I.e. we obtain 5 sets of measurements total, each having been averaged 10 times. All velocities are normalized by dividing all values by the maximum velocity recorded. The normalization increases numerical precision of floating point numbers in case of very high measurement numbers, and helps in having the optimal regularization parameter be of similar values for different systems, which will be introduced in section 2.7. As a result, the following plots such as Figure 3 use unitless velocities, and may not be consistent between different plots such as Figure 4b due to having a different global maxima chosen between different scripts. The normalization does not affect the results.

After calibration, a 1 cm<sup>3</sup> iron cube is bonded to the plate to simulate a defect. During monitoring, we excite each transducer again but measure only at the transducer locations. In our setup, the LDV acquires these sparse responses at the transducer positions.

For future discussion regarding sub-wavelength localization, we roughly estimate the dispersion properties of the CFRP plate. We extract an x-t slice along the x-axis at y=6.2cm through the active transducer from Figure 3 and window the time axis to exclude edge reflections (Figure 4a). We then compute a 2D FFT to obtain the  $k$ - $\omega$  spectrum. Selecting the peak-energy wavenumber  $k^*(f)$  for each frequency yields the phase velocity  $v_p(f) = 2\pi f/k^*(f)$  and wavelength  $\lambda(f) = 2\pi/k^*(f)$  (Figure 4b). See Appendix A.4 for further comments regarding the validity of the phase velocities.

## 4. Results

We first present a baseline simulation (Case A) to illustrate the method under controlled conditions. We then provide experimental validation using the setup described in Section 3. Finally, we present additional simulations that probe limits and variants of the approach.

Raw data with emitter 5 at time 0.17 ms

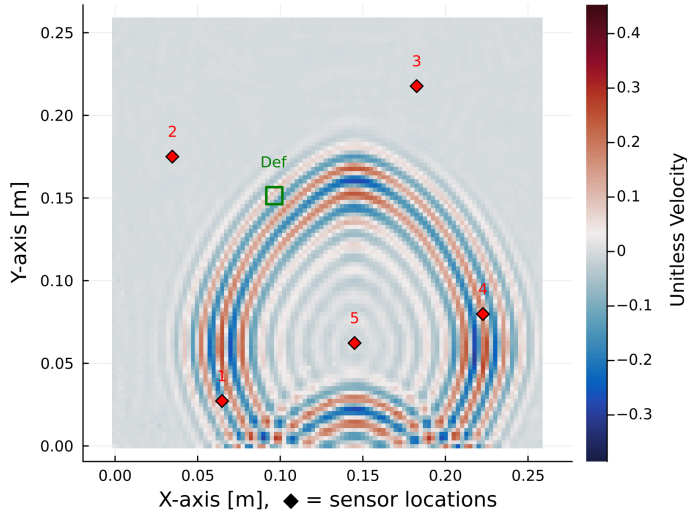
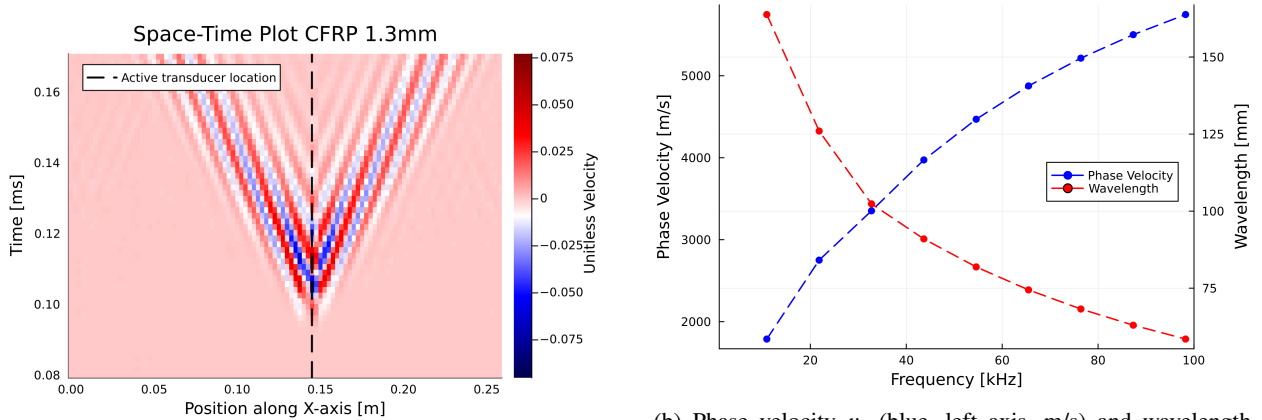


**Figure 3:** Snapshot of the measured wavefield propagating in the CFRP plate at  $t = 0.17$  ms, lowpass filtered to 150 kHz. Red diamonds mark the five transducers (numbered 1–5). Transducer 5 is the active source in this instance. The green square indicates the location where the defect was bonded in the monitoring phase (not yet present in this calibration scan). Note: The results in this paper employ 1–50 kHz bandpass filtering, which significantly distorts the pulse shape compared to this view. (See Appendix A.2.)



(a) Space-time diagram along the  $y = 6.2\text{cm}$  plane through the active sensor nr 5, derived from the same data as Figure 3.

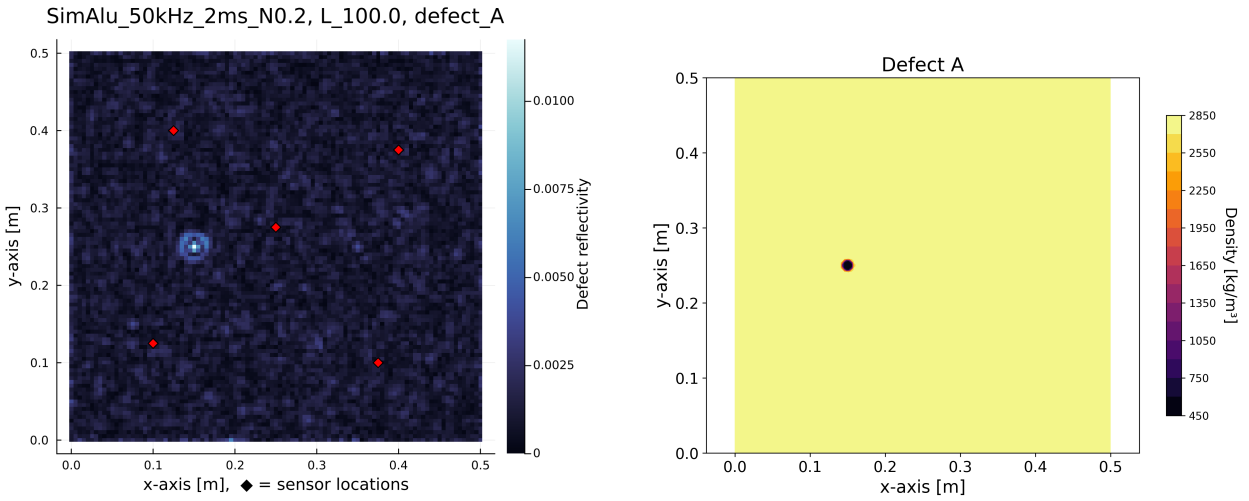
(b) Phase velocity  $v_p$  (blue, left axis, m/s) and wavelength  $\lambda$  (red, right axis, mm) versus frequency  $f$  (kHz). Due to anisotropy, the values are to be seen as approximate.

Figure 4: Empirical dispersion of the CFRP plate from the calibration scan.

#### 4.1. Results - Simulations (Case A)

The method was validated using the spectral-element modelling suite Salvus [22]. We simulated elastic wave propagation on a 50 cm  $\times$  50 cm, 9 mm-thick rectangular aluminum plate, with defects modelled as localized density reductions.

Figure 5a shows the reconstructed defect vector  $\vec{d}$ , visualized as a heatmap of its magnitude at each spatial grid point (LDV measurement location). Solving equation 14 yields a complex-valued coefficient at every grid point, interpreted



(a) Reconstructed defect amplitude for simulated case A in the 0–50 kHz band, showing accurate localization of a single 1.5 cm inclusion under 20% RMS noise.

(b) Ground-truth density map for case A, with a tapered circular lower-density inclusion of 1.5 cm diameter and relative density 0.2.

**Figure 5:** Simulation case A with a single small inclusion. Left: reconstructed defect amplitude obtained with the empirical-operator inversion. Right: corresponding ground-truth density map.

here as a local reflection amplitude. In this experiment,  $\vec{d}$  contains  $100 \times 100 = 10,000$  entries. For visualization, the 1D indexing is mapped back to the original 2D scan grid. Since the plot shows  $|\vec{d}|$ , phase information is not displayed.

Figure 5 shows a tapered circular lower-density inclusion of 1.5 cm diameter with relative density 20%. This baseline case serves as a reference for comparison with subsequent results. The driving pulse is a 50 kHz central-frequency Ricker wavelet with a 2 ms repetition period; the configuration uses 5 sensors, 20% Gaussian RMS noise, and a 0–50 kHz low-pass filter.

## 4.2. Results - Experimental Validation

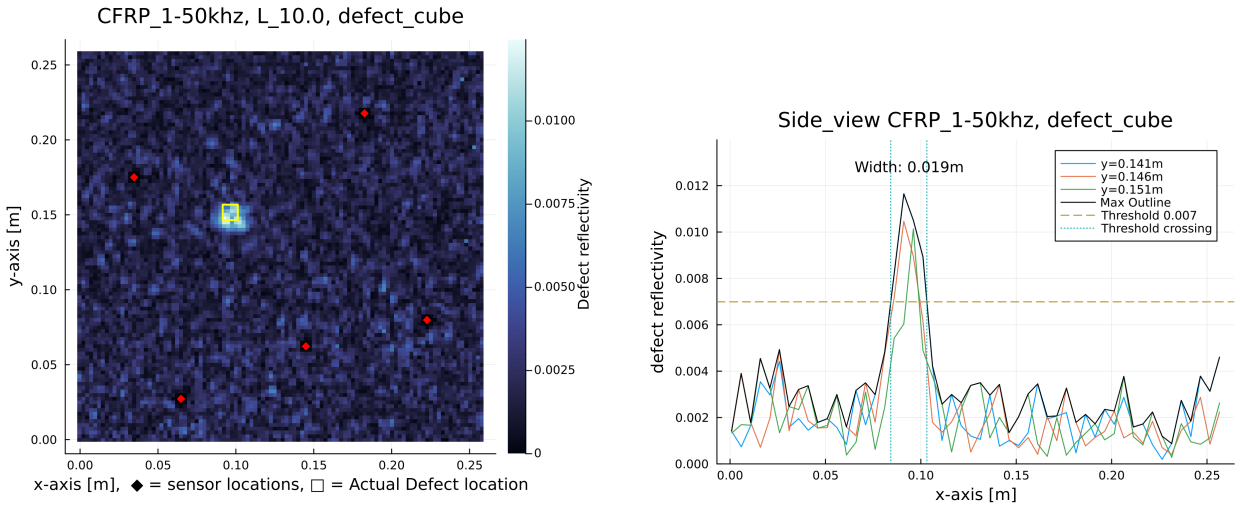
The method is validated experimentally on the CFRP plate described in 3. The experimental parameters are similar to the simulated case: a 2 ms repetition period, excitation by an 80 kHz Ricker wavelet, and bandpass filtering to 1–50 kHz.

A  $1 \times 1 \times 1$  cm<sup>3</sup> iron cube is localized using sparse measurements at the five transducer locations.

The reconstruction in Figure 6a localizes a pronounced response near the defect location (yellow square). The black regions around each transducer (red diamonds) indicate exclusion zones, corresponding to the unpenalized region in the regularization (Section 2.7) and masked in the visualization. Without this masking, these areas exhibit large reconstructed values that primarily reflect systematic experimental differences (e.g., pulse-amplitude changes between calibration and monitoring) rather than defect scattering.

Figure 6b provides cross-sectional views along the x-axis. Slices exceeding 0.6 times the maximum amplitude are retained and used to draw an envelope. Using this criterion, the defect signature exhibits a half-width of approximately 2 cm.

To probe the low-frequency limit, we also evaluate the 1–15 kHz band (audible range). Running the calculation on the full  $104 \times 104$  grid yields mixed results (Appendix A.3). We therefore reduce the reconstruction grid to  $50 \times 50$  by using the same dataset as above but restricting the inversion to a subgrid. The corresponding reconstruction is shown in Figure 7 and yields a compact defect signature at 15 kHz with an estimated FWHM of  $\approx 1.4$  cm, despite a wavelength on the order of  $\approx 16$  cm in this band.



(a) Reconstructed magnitude of the defect vector  $|\vec{d}|$  in the 1–50 kHz band. Red diamonds mark the five transducer locations. The yellow square indicates the location where the iron cube was bonded. The black regions around transducers are the unpenalized exclusion zones from the regularization.

(b) Cross-sectional profiles along the x-axis through the reconstructed defect (left panel). Colored envelopes show slices with amplitude exceeding 0.6 times the maximum. The localization width is estimated from the 0.6 amplitude threshold, yielding a half-width of approximately 2 cm.

**Figure 6:** Defect localization results in the 1–50 kHz band using sparse transducer measurements. Left: full 2D reconstruction showing sub-wavelength localization of the defect. Right: cross-sectional analysis quantifying the localization width.

#### 4.3. Results - Additional Simulations

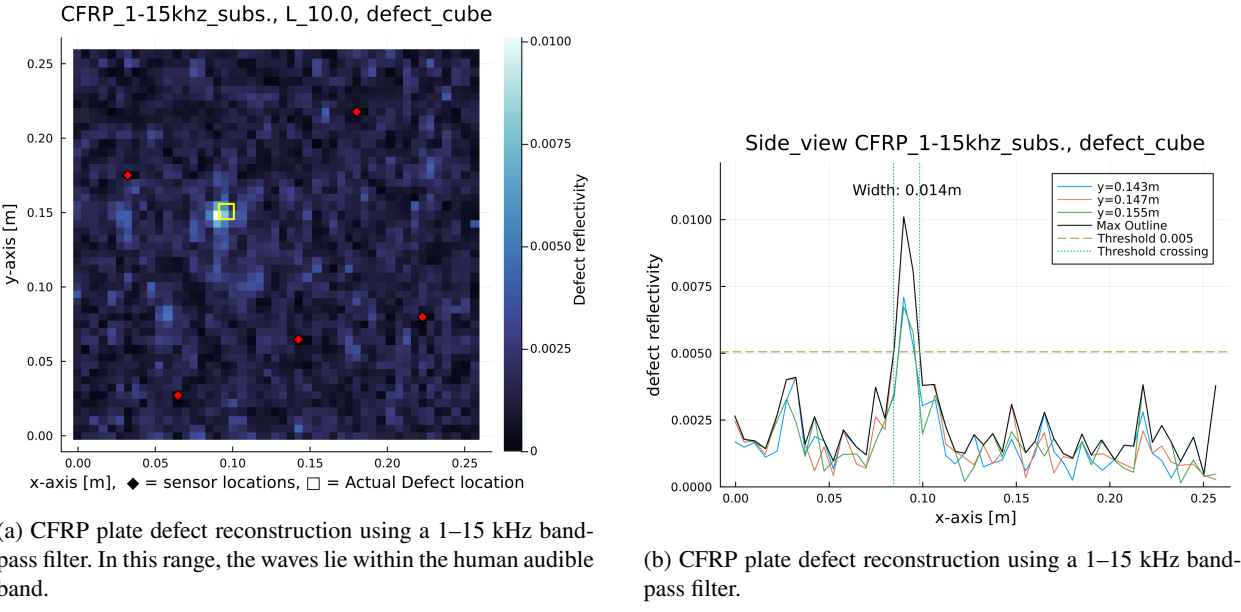
To complement the baseline simulation (Case A, Section 4.1) and the experimental validation above, we consider additional simulated cases that probe variants and practical limits of the approach. Unless explained otherwise, the simulation setup is identical to Section 4.1.

**Case A5B\_1:** Figure 8 contains two tapered inclusions of 1.5 cm and 5 cm diameter at relative density 0.2, using the same parameters as before section 4.1. This case demonstrates that the method can discern multiple defects and larger shapes, despite internally assuming single scattering. The reconstruction quality degrades through pronounced background artifacts, consistent with a scenario that departs from conditions well described by single scattering.

**Case A5B\_2:** In Figure 9a, the same defect as in 8 is simulated with a 5 ms period and 0–100 kHz frequency range. The algorithm therefore has access to five times more temporal information ( $2 \times$  higher frequency,  $2.5 \times$  longer period) than in the previous cases. We observe improved reconstruction fidelity and reduced background artifacts. This result suggests that increased temporal bandwidth and a longer listening window can sharpen the reconstruction and suppress background, while a systematic analysis of these effects is deferred to [33].

**Case ECHO:** Figure 9b provides a proof of concept that the method can operate using only one sensor. In this case, a single transducer is active as emitter and simultaneously acts as the only sensor (pulse-echo configuration). The data are bandpass filtered to 0–100 kHz with a 5 ms period and 10% RMS noise; all other parameters are the same as in the other simulation cases. The reconstructed defect more closely resembles the small-defect result in Figure 9a than 5a, suggesting that localization is primarily controlled by frequency content rather than the number of sensors. More complex defects such as 8b (not shown here) reconstruct poorly in this echo configuration; performance is also more sensitive to noise and degrades substantially at lower frequencies. These observations are consistent with [17], where increased sensor counts reduce "contrast" (called "background artifacts" here) but do not improve resolution in the same way as higher frequencies. The problem setting is similar to [9, 8], providing a comparison to alternative approaches. Evaluation attempts using real-world data did not yield interpretable results, consistent with the simulations performing poorly under the same low-frequency, short-period constraints.

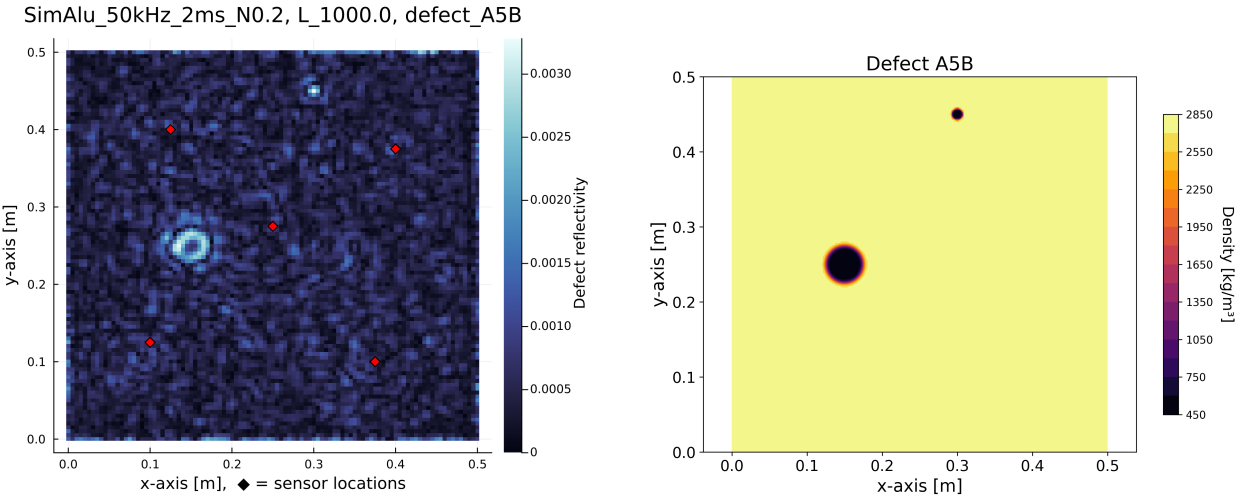
Further details and additional simulation examples are documented in Appendix [33].



(a) CFRP plate defect reconstruction using a 1–15 kHz band-pass filter. In this range, the waves lie within the human audible band.

(b) CFRP plate defect reconstruction using a 1–15 kHz band-pass filter.

**Figure 7:** Cross-sectional profiles along the x-axis through the reconstructed defect (left panel). Colored envelopes show slices with amplitude exceeding 0.5 times the maximum. The localization width is as estimated as the FWHM threshold, at 1.4 cm.



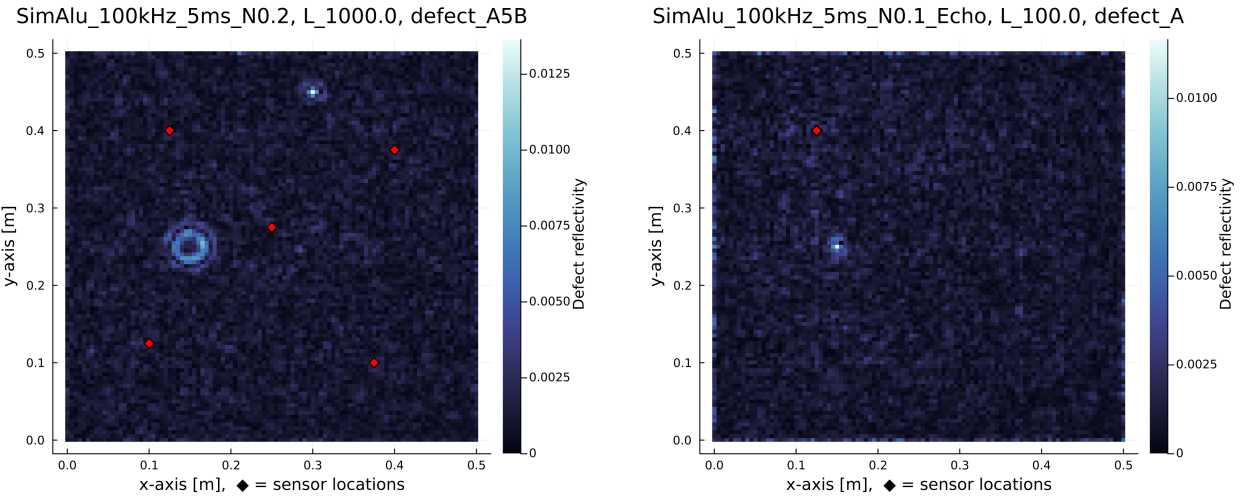
(a) Reconstructed defect amplitude for simulated case A5B with two inclusions, resolving the 1.5 cm and 5 cm defects but showing increased background artifacts.

(b) Ground-truth density map for case A5B, containing two tapered circular lower-density inclusions with diameters of 1.5 cm and 5 cm at relative density 0.2.

**Figure 8:** Simulation case A5B with two inclusions. Left: reconstruction illustrating simultaneous localization of both defects and the emergence of background artifacts. Right: ground-truth density map used as reference.

## 5. Discussion

Experimental validation on the CFRP plate (Section 4.2) demonstrates defect localization using the calibration-to-monitoring procedure and sparse measurements at the transducer locations. In the 1–50 kHz reconstruction, the defect signature has a half-width of approximately 2 cm. Relative to a wavelength of  $\lambda_{50} \approx 8$  cm at 50 kHz (Figure 4), this corresponds to sub-wavelength localization; its origin and interpretation are discussed further in Appendix B.2. In



(a) Reconstruction of case A5B using 5 ms period and 0–100 kHz bandwidth, demonstrating reduced background artifacts and sharper localization compared to Fig. 8.

(b) Single-transducer pulse-echo reconstruction of the small defect from case A (Fig. 5), using 0–100 kHz bandwidth with 10% RMS noise.

**Figure 9:** Simulation cases with extended frequency range and reduced sensor count. Left: case A5B\_2 at 0–100 kHz shows improved reconstruction fidelity. Right: pulse-echo configuration (case ECHO) successfully localizes defect A using a single transducer.

addition, the very-low-frequency evaluation in the 1–15 kHz band (Figure 7) yields an estimated FWHM of  $\approx 1.4$  cm at a wavelength on the order of  $\approx 16$  cm, demonstrating strong localization even in the audible range.

The absolute pixel values of all results in section 4 should be interpreted as relative indicators of defect location rather than quantitative scattering amplitudes, since the regularization parameter  $\lambda$  influences amplitude scaling. In future implementations, this dependence could be addressed by characterizing the amplitude change induced by regularization and by correcting for the density of grid points in the model.

In the experimental dataset, extending the bandwidth from 1–50 kHz to higher frequencies yields only marginal improvement and degrades markedly at frequencies over 100 kHz. Since this behavior is not observed in the simulated cases, it suggests that the high-frequency data are more susceptible to errors introduced by real-world implementation details. Because the method performs well in lower-frequency bands, such sensitivities can be partially circumvented, supporting robustness in practical implementations. For further discussion, see Appendix B.1.

The 1–15 kHz experiments also highlight a practical conditioning effect: when the number of free defect parameters is too large relative to the information content of the data, the reconstruction can develop isolated high-amplitude pixels (Appendix A.3). In this work, using the full  $104 \times 104$  defect grid (10 816 unknowns) with a measurement vector of length 300 produced mixed results, whereas restricting the inversion to a  $50 \times 50$  subgrid (2 500 unknowns) yielded a stable, compact peak. This behavior suggests that reconstruction quality depends on the joint ratio between spatial degrees of freedom and effective data constraints (set by bandwidth, period length, and sensor configuration), and/or by grid density and frequency. A more precise characterization of this trade-off would require systematic parameter studies in future work.

The experimental validation is comparable to the baseline simulation (Sections 4.1, 4.2) with respect to the periodic excitation (2 ms repetition period), sparse measurements at 5 transducers, and band-limited processing in the 0–50 kHz range. The experimental setup deviates slightly by restricting the lower band to 1–50 kHz due to systematic measurement noise at very low frequencies and by using a different means to induce a small defect. This overall consistency supports using the simulation setup as representative of the method under comparable bandwidth and sparsity, while retaining the advantages of controlled ground truth and tunable noise.

The additional simulations (Section 4.1) complement the results above. Case A5B\_1 indicates that multiple and larger inclusions can be localized simultaneously, but that background artifacts increase as scenarios depart from the single-scattering approximation. Case A5B\_2 shows that increased temporal information (longer period and higher-frequency content) can improve reconstruction fidelity and reduce artifacts, representing a hypothetical idealized implementation. Case ECHO provides a proof of concept for localization with a single transducer.

Limitations remain: large defects with relative size  $\approx 0.1$  become difficult to resolve when single scattering breaks down. While small defects can be localized well below the wavelength, accurate shape recovery is not expected when they are much smaller than the wavelength [33]. In addition, the experimental defect is an adhered metal cube and thus differs from realistic CFRP damage such as delaminations. However, the cube defect serves as a useful proxy for contact-based applications, and the computational efficiency after calibration (Appendix C.1) suggests viability for both frequent automated SHM and low-cost touchscreen implementations [17].

## 6. Conclusion

This paper presented and experimentally validated an empirical, fully vectorized linear-operator framework for inverse scattering and structural health monitoring. Using bonded, low-cost piezoelectric transducers and a one-time LDV calibration scan, we constructed source–receiver impulse-response operators on a discrete periodic time axis, represented propagation as DFT-diagonalizable circular convolution, and posed defect localization as a Tikhonov-regularized linear inverse problem. On an anisotropic CFRP plate, an adhered  $1\text{ cm}^3$  iron cube was localized from sparse measurements at the transducer locations, consistent with sub-wavelength localization, with a width of about 2 cm at a minimum wavelength of about 8 cm and, in a very-low-frequency 1–15 kHz band, an estimated FWHM of  $\approx 1.4$  cm at a wavelength on the order of  $\approx 16$  cm. Complementary simulations on an aluminum plate demonstrated accurate localization of small inclusions, discrimination of multiple defects and defect shapes, and proof-of-concept operation in a single-sensor echo configuration.

The framework is general and modular: it does not rely on a detailed forward model and can, in principle, be applied to other defect models, sensing layouts, and wave-bearing media, provided linearity and time invariance hold. Operating in the 1–50 kHz band, and despite pulse-shape drift and LDV misalignment, the results support the central premise that empirical operators can absorb many experimental imperfections while retaining sub-wavelength localization. At the same time, limitations remain, including the single-scattering assumption, the simple delta-like defect basis, and reliance on LDV for calibration. These point to natural future work on richer scattering models and fully transducer-based implementations, toward practical SHM systems in which the one-time calibration enables fast, low-cost monitoring, possibly including touch-like sensing applications.

## A. Additional experimental details and preprocessing

This appendix documents measurement-component choices, filtering effects induced by the periodic-time formulation, and approximate dispersion estimation used only for order-of-magnitude wavelength references.

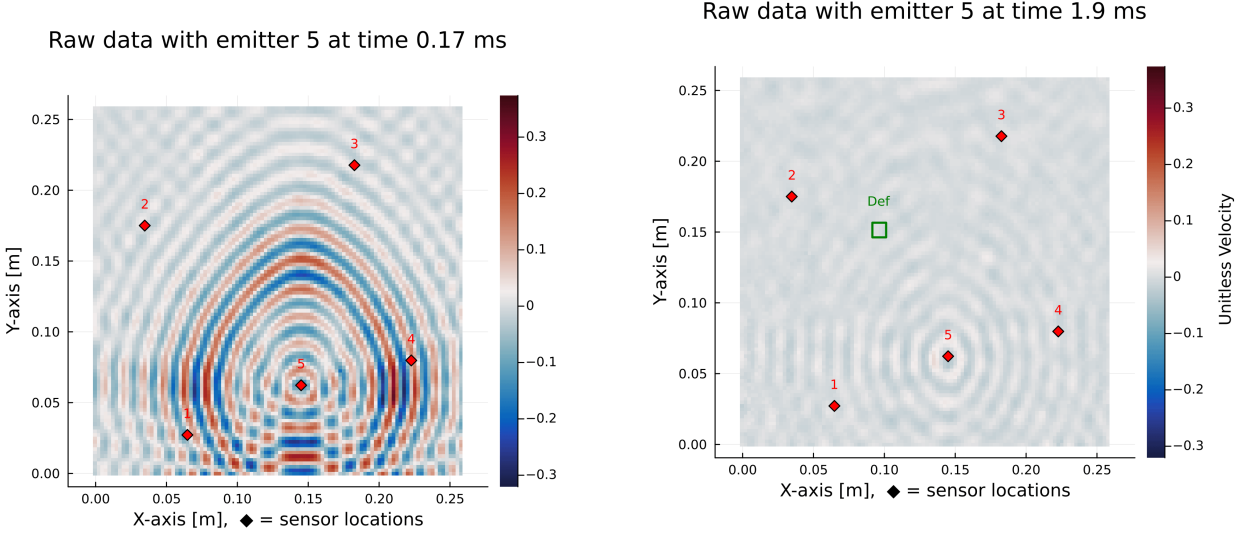
### A.1. Longitudinal Velocity Components

In this work we use only the out-of-plane LDV velocity component  $V_z$ , which is excited most strongly by the bonded piezoelectric discs and yields the highest signal-to-noise ratio in our dataset. However, the proposed framework is not specific to Lamb-wave mode content or to any particular velocity component: it operates on an empirically calibrated linear time-invariant input–output map, and can in principle be applied to any linear time-independent measured observable (e.g.,  $V_x$ ,  $V_y$ ,  $V_z$ , their sum or transducer voltage).

We did not evaluate multi-component reconstructions in the simulations. In the experimental data, the in-plane components ( $V_x$ ,  $V_y$ ) exhibited substantially lower SNR and contained many grid points with missing or unreliable measurements, leading to non-interpretable reconstructions. For this reason, we restrict the experimental results in this paper to  $V_z$ .

### A.2. Effect of 1–50 kHz filtering under periodic time

The results presented in the main paper employ a 1–50 kHz bandpass filter, whereas the calibration snapshot in Figure 3 is unfiltered. Figure 10a shows the same acquisition time point after low-pass filtering to 50 kHz. The filtering substantially increases the effective pulse duration, such that the response wraps around within the periodic time



(a) CFRP plate response at  $t = 0.17$  ms, bandpass filtered to 1–50 kHz. Transducer 5 is active. Compared to the unfiltered snapshot in Figure 3, the pulse is broadened by the low-pass filtering.

(b) Same setup at  $t = 1.9$  ms, near the end of the 2 ms period. The pulse tail from the current repetition is still visible, and the pulse from the next repetition (nominally starting at  $t = 0.12$  ms) is already present, demonstrating the wraparound inherent in the periodic time treatment.

**Figure 10:** Effect of 1–50 kHz bandpass filtering on the transducer pulse shape in the periodic time framework.

window. Accordingly, near the end of the 2 ms period ( $t \approx 1.9$  ms), the pulse from the subsequent repetition is already visible (Figure 10b). This observation highlights that the framework does not require short, well-separated pulses; the periodic time treatment is therefore not merely a computational convenience but is intrinsic to the formulation of the inverse problem.

### A.3. Very-low-frequency evaluation (1–15 kHz and 1–30 kHz)

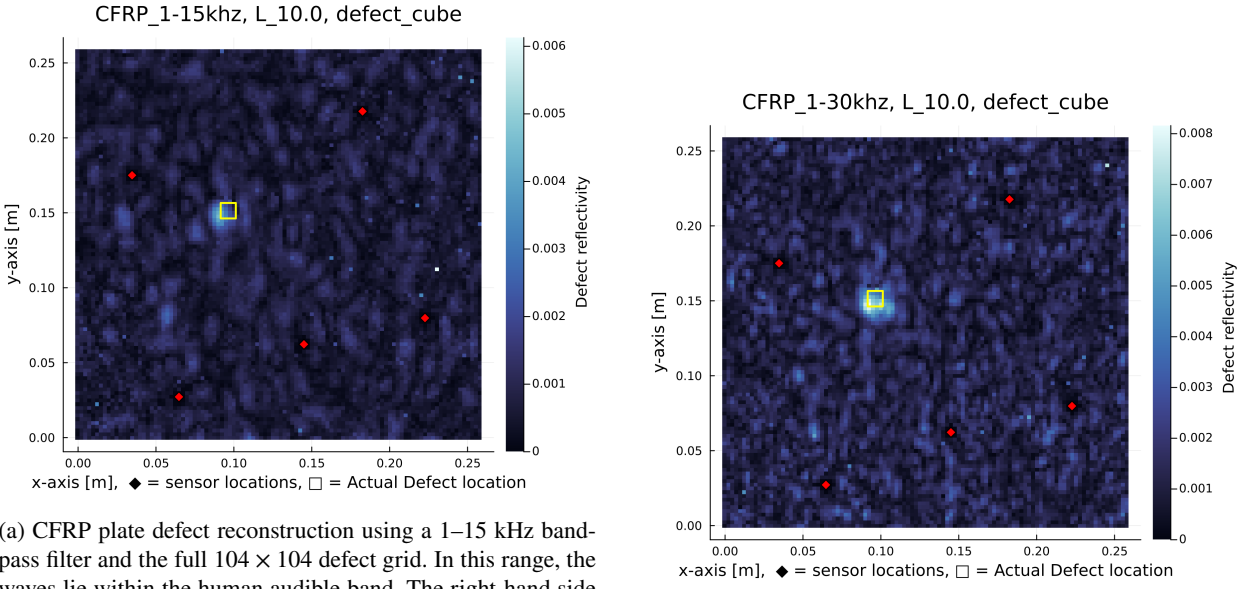
To probe the low-frequency limit using the original full-resolution defect space, we evaluate the 1–15 kHz and 1–30 kHz bands on the full  $104 \times 104$  defect grid (10,816 unknowns). From Figure 4a, the corresponding minimum wavelengths are on the order of 16 cm and 10 cm, respectively.

The resulting reconstructions in Figure 11 illustrate how the inversion degrades at very low frequencies when too many defect parameters are left free. In the 1–15 kHz panel (left), the defect region is still roughly identifiable, but the image is dominated by background artifacts and isolated high-amplitude pixels, particularly on the right-hand side of the reconstruction. Similar behavior is observed in the 1–30 kHz case to a smaller extend. These pixel-scale spikes seem to indicate a highly underdetermined system or too low frequencies, in which the number of free defect parameters is too large relative to the information content of the data. In contrast, restricting the inversion to a  $50 \times 50$  subgrid in the main text (Figure 7) yields a stable, compact peak at 15 kHz.

### A.4. Dispersion estimate and limitations

Figures 4 suggest phase velocities that increase with frequency and reach values on the order of 7 km/s at the upper end of the measured band. A theoretical Lamb-mode estimate[10], using approximate CFRP parameters, places the high-frequency A0 branch near 3.8 km/s. This theoretical calculation is only a rough reference because it assumes isotropic, homogeneous material properties and does not account for the plate's anisotropy or layup; substantial discrepancies are therefore expected. Neither approach alone provides a definitive “ground truth.” The mismatch could also reflect a systematic error in the dispersion-processing workflow. The relevant code can be found in [33].

For the purposes of this paper, we use phase-velocity/wavelength estimates only as order-of-magnitude references when assessing whether the observed localization is sub-wavelength. At 50 kHz, the corresponding wavelengths are



(a) CFRP plate defect reconstruction using a 1–15 kHz bandpass filter and the full  $104 \times 104$  defect grid. In this range, the waves lie within the human audible band. The right-hand side of the image shows isolated high-amplitude pixels, indicative of an overparameterized defect space.

(b) CFRP plate defect reconstruction using a 1–30 kHz bandpass filter with the same  $104 \times 104$  defect grid.

**Figure 11:** Defect localization results in the very low 1–15 kHz and 1–30 kHz bands using the full  $104 \times 104$  defect grid. Although the defect region remains broadly identifiable, the reconstructions exhibit pronounced background artifacts and isolated high-amplitude pixels (especially on the right-hand side of the 1–15 kHz image), consistent with too many free defect parameters relative to the available data. Compare with the subsampled  $50 \times 50$  reconstruction in Figure 7.

on the order of a few centimeters, and the observed localization ( $\approx 2$  cm) remains smaller than both the theoretical estimate of 4cm and the experimental estimate of 8cm.

## B. Additional diagnostics and limitations

This appendix collects observations that affect reconstruction quality but are not central to the core method description.

### B.1. High-frequency degradation in the experiment

In the experimental example of section 4.2, including higher-frequency data provides limited incremental benefit, even though the measured wave spectrum extends beyond 50 kHz. This is consistent with the 80 kHz central frequency of the transmitted pulses and is confirmed by measurements at multiple locations on the plate.

Using the 100–150 kHz band alone yields poor results, suggesting that this frequency range does not contribute useful information for defect localization in the current setup. It is also notable that processing 1–50 kHz performs similarly to 1–80 kHz, despite the system matrix in equation 14 having dimensions  $1000 \times 10816$ . The inverse problem is therefore highly underdetermined (by a factor  $> 10$ ), so the absence of improvement from additional bandwidth is nontrivial.

Because this high-frequency degradation is not observed in the simulated results [33], a likely contributor is misalignment between calibration and monitoring. During calibration, the LDV scans a dense  $104 \times 104$  grid; during monitoring, it measures only at the transducer locations, and repositioning relies on visual cues, which can introduce small spatial offsets. Such offsets couple strongly to phase at shorter wavelengths. This issue would be avoided if monitoring were performed using the transducers themselves as receivers rather than the LDV, as discussed in Section C.3.

Alternatively, the discrepancy may reflect limitations of the defect model. In Section 2.5, defects are assumed to exhibit a delta-like response, i.e., an instantaneous and frequency-independent reflection. In the simulations, defects

were modeled as density perturbations, whereas the experimental defect (an adhered metal cube) is more representative of a stiffness perturbation, for which the delta-like assumption may be less appropriate.

Restricting the frequency band may therefore be advantageous: although fewer data are used, the modeling assumptions only need to hold over a narrower band. However, the present experimental setup does not allow these effects to be isolated, so no definitive conclusion can be drawn.

## B.2. Sub-Wavelength localization discussions

The Sub-Wavelength localization has generated a lot of discussion, yet it remains challenging to provide a concise explanation, especially since it is difficult to demonstrate a limitation does *not* occur. Based on the mathematical methodology used which does not rely on explicit spatial information, there appears to be no inherent restriction enforcing a wavelength limit. In contrast, other methods often have such restrictions, typically due to the need to reconstruct measured waves in space. For example, [9] describes a method with such a limitation, though it is not explicitly discussed there.

However, in the simulation study here, a decrease in resolution is observed at lower frequencies, which suggests that the method is not entirely independent of wavelength-related limits. The discussion is complicated by the fact that changing the frequency bandwidth simultaneously affects three factors: the maximum frequency, the amount of information available due to the system matrix shape (see Eq. 14), and increased susceptibility to standard norm-based regularization, which can smear the result because neighboring points respond more similarly at longer wavelengths. For all intents and purposes, the method does have a resolution limitation as a function of frequency, but it is also dependent on other variables, without a hard cutoff based on frequency alone. Given the proof-of-concept nature of this paper, we refrain from exploring this topic in depth, simply noting that it is possible to isolate each variable to obtain definite answers if desired.

## C. Implementation details and extensions

This appendix summarizes computational scaling, the sensor-pair stacking used, and straightforward extensions of the defect parameterization.

### C.1. Computational performance

In the implementation used in this paper, the global system matrix  $\mathcal{L}_{\text{full}}$  from equation 14 is formed explicitly and inverted in a Tikhonov sense via  $(\mathcal{L}^T \mathcal{L} + \lambda \Gamma)^{-1} \mathcal{L}^T$ . For a matrix of size  $n \times m$  with measurements  $n$  and defect parameters  $m$  (equals grid size in our case), memory scales as  $\mathcal{O}(nm)$  and the inversion cost as  $\mathcal{O}(nm^2)$ . Adding measurements is therefore comparatively cheap, whereas enlarging the defect space is the dominant computational bottleneck. On a standard laptop with 16 GB RAM (about 9 GB effectively usable) and an Intel Gen13 i7 CPU, practical limits are matrices of order  $10^4 \times 10^4$  in Float32. For the experimental CFRP case studied here ( $\approx 10^4$  defect parameters and  $\approx 10^3$  measurements), the one-time inversion of  $\mathcal{L}_{\text{full}}$  takes about 17 s. The empirical impulse responses (Section 2.4) are obtained in roughly 4 s and scale linearly in grid size and transducer count, so they remain inexpensive compared to the inversion as the scale increases. The subsequent evaluations for new measurement vectors reduce to a single matrix–vector multiplication and take around 3–5 ms in the presented case. From a computational perspective, this separation between a moderately expensive calibration step and very fast evaluation makes the method potentially viable as a low-cost, touchscreen application as in [17]. The evaluation does not have any memory requirements, potentially allowing frequent automated SHM on a simple system.

### C.2. Sensor Configurations

The sensor configuration used in this paper (Section 2.6) is [[1,2], [1,3], [1,4], [1,5], [2,3], [2,4], [2,5], [3,4], [3,5], [4,5]]. For the echo configuration in Figure 9b, it is [[1,1]]. The 5-sensor configuration is chosen to avoid including symmetric pairs such as [[1,2],[2,1]], which, under the reciprocity assumption, are expected to provide limited additional information. Testing confirmed this behavior.

In hindsight, a layout such as [[1,2], [1,3], [2,3], [2,4], [3,4], ...] may better balance the roles of the emitters. This was considered too late for the present study. Follow-up tests did not reveal noticeable improvements, and the original configuration was retained.

Including a full set of measurements, including self-measurements such as ([1,1],[2,2] etc.), should in principle improve the reconstruction. However, in our tests it tended to reduce reconstruction quality. This behavior is unexpected given that the single-pulse case in Figure 9b is functional, and suggests that the additional channels may introduce systematic effects that are not captured by the present formulation.

### C.3. Toward fully transducer-based monitoring

A fully transducer-based implementation could proceed as follows. At each transducer location, two transducers are placed in close proximity: one acting as the transmitter and one as the sensor. During calibration, a transmitting transducer emits a periodic pulse while an LDV scans the object. The sensing-transducer measurement is appended to the LDV grid-scan dataset and treated as an additional grid point. In the implementation, this measurement is assigned to the emitter location so that transducer-specific coupling effects of both transducers are absorbed into the empirically calibrated operators, potentially enabling the use of inexpensive transducers with imperfect coupling.

**Notes:** Thick, cube-shaped transducers should be avoided, as their stiffness locally alters the plate and makes measurement at or by the transducer impossible. Flat, plate-like ceramic transducers should be used relative to the plate thickness.

It is important to note that the physical location of the emitting transducer and the modeled transmitter location may not coincide. This is intentional and consistent with the approach in this paper, since the LDV does not scan exactly at the transducer positions.

### C.4. Generalization to arbitrary defect bases

The results shown in this paper use the simple delta basis. The approach can be generalized to arbitrary defect basis vectors, including multiple basis vectors per grid location.

Assuming we have obtained empirical defect vectors for two defect types of interest,  $\vec{b}_1$  and  $\vec{b}_2$ , we can implement these two vectors as a basis using a projector matrix  $P$ :

$$P := \begin{bmatrix} \vec{b}_1 & \vec{b}_2 \end{bmatrix} \quad (17)$$

Replacing  $\vec{e}_0$  in 12, we obtain

$$L_{ij} := [ G_{i1}G_{1j}S_j P \mid G_{i2}G_{2j}S_j P \mid \dots \mid G_{iN}G_{Nj}S_j P ], \quad (18)$$

with a corresponding adjustment to the full defect vector  $\mathbf{d}$  to hold two parameters per location.

$$\mathbf{d} := \begin{bmatrix} d_{1,1} \\ d_{1,2} \\ d_{2,1} \\ \vdots \\ d_{N,2} \end{bmatrix} \quad (19)$$

where for  $d_{k,b}$ ,  $k$  denotes the grid location and  $b$  the basis vector index at that location.

This generalized formulation is not used in this paper, since we continue using the delta-like defect basis. Simulation experiments to date have not identified alternative bases that provide a clear performance gain relative to their added computational cost. However, richer local bases may be required to improve sensitivity to CFRP delaminations, which may not exhibit a strongly delta-like temporal response; one possible route is to empirically measure the response of a delaminated region and use it as a basis vector [33].

## References

- [1] Bazulin, E., Goncharsky, A., Romanov, S., Seryozhnikov, S., 2019. Inverse problems of ultrasonic tomography in nondestructive testing: Mathematical methods and experiment. Russian Journal of Nondestructive Testing 55, 453–462. doi:10.1134/S1061830919060020.
- [2] Calomfirescu, M., 2008. Lamb Waves for Structural Health Monitoring in Viscoelastic Composite Materials. Science-Report aus dem Faserinstitut Bremen, Logos-Verlag. URL: [https://books.google.ch/books?id=\\_p6muhbVB0C](https://books.google.ch/books?id=_p6muhbVB0C).
- [3] Cawley, P., 2002. Practical long range guided wave inspection - applications to pipes and rail, Chennai.

- [4] Celli, P., Porfiri, M., 2022. The detection matrix as a model-agnostic tool to estimate the number of degrees of freedom in mechanical systems and engineering structures. *Chaos: An Interdisciplinary Journal of Nonlinear Science* 32. URL: <http://dx.doi.org/10.1063/5.0083767>, doi:10.1063/5.0083767.
- [5] Chen, S., Thompson, A., Dodwell, T., Hallett, S., Belnoue, J., 2025. A comparison between robust design and digital twin approaches for non-crimp fabric (ncf) forming. *Composites Part A: Applied Science and Manufacturing* 193, 108864. URL: <https://www.sciencedirect.com/science/article/pii/S1359835X25001587>, doi:<https://doi.org/10.1016/j.compositesa.2025.108864>.
- [6] Chia, C.C., Lee, S.Y., Harmin, M.Y., Choi, Y., Lee, J.R., 2023. Guided ultrasonic waves propagation imaging: a review. *Measurement Science and Technology* 34, 052001. URL: <https://iopscience.iop.org/article/10.1088/1361-6501/acae27>, doi:10.1088/1361-6501/acae27.
- [7] Derusova, D.A., Vavilov, V.P., Druzhinin, N.V., Shpil'noi, V.Y., Pestryakov, A.N., 2022. Detecting defects in composite polymers by using 3d scanning laser doppler vibrometry. *Materials* 15. URL: <https://www.mdpi.com/1996-1944/15/20/7176>, doi:10.3390/ma15207176.
- [8] Draeger, C., Fink, M., 1997. One-channel time reversal of elastic waves in a chaotic 2d-silicon cavity. *Phys. Rev. Lett.* 79, 407–410. URL: <https://link.aps.org/doi/10.1103/PhysRevLett.79.407>, doi:10.1103/PhysRevLett.79.407.
- [9] Ebrahimkhani, A., Salamone, S., 2017. Acoustic emission source localization in thin metallic plates: A single-sensor approach based on multimodal edge reflections. *Ultrasonics* 78, 134–145. doi:10.1016/j.ultras.2017.03.006.
- [10] Francisco Rotea, I., . URL: <https://github.com/franciscorotea/Lamb-Wave-Dispersion?tab=readme-ov-file>.
- [11] Fu, Y., Yao, X., 2022. A review on manufacturing defects and their detection of fiber reinforced resin matrix composites. *Composites Part C: Open Access* 8, 100276. URL: <https://www.sciencedirect.com/science/article/pii/S266668202200041X>, doi:<https://doi.org/10.1016/j.jcomc.2022.100276>.
- [12] Fuhr, M., Reichel, L., 2012. A new Tikhonov regularization method. *Numerical Algorithms* 59, 433–445. URL: <https://doi.org/10.1007/s11075-011-9498-x>, doi:10.1007/s11075-011-9498-x.
- [13] Golub, G., Heath, M., Wahba, G., 1979. Generalized cross-validation as a method for choosing a good ridge parameter. *Technometrics* 21, 215–223. doi:10.1080/00401706.1979.10489751.
- [14] Han, S., Li, Q., Cui, Z., Xiao, P., Miao, Y., Chen, L., Li, Y., 2024. Non-destructive testing and structural health monitoring technologies for carbon fiber reinforced polymers: a review. *Nondestructive Testing and Evaluation* 39, 725–761. URL: <https://doi.org/10.1080/10589759.2024.2324149>, doi:10.1080/10589759.2024.2324149, arXiv:<https://doi.org/10.1080/10589759.2024.2324149>.
- [15] Hansen, P.C., 2010a. 4. Computational Aspects: Regularization Methods. SIAM. pp. 53–83. URL: <https://epubs.siam.org/doi/abs/10.1137/1.9780898718836.ch4>, doi:10.1137/1.9780898718836.ch4, arXiv:<https://epubs.siam.org/doi/pdf/10.1137/1.9780898718836.ch4>.
- [16] Hansen, P.C., 2010b. 5. Getting Serious: Choosing the Regularization Parameter. SIAM. pp. 85–107. URL: <https://epubs.siam.org/doi/abs/10.1137/1.9780898718836.ch5>, doi:10.1137/1.9780898718836.ch5, arXiv:<https://epubs.siam.org/doi/pdf/10.1137/1.9780898718836.ch5>.
- [17] Ing, R.K., Quieffin, N., Catheline, S., Fink, M., 2005. In solid localization of finger impacts using acoustic time-reversal process. *Applied Physics Letters* 87, 204104. URL: <https://doi.org/10.1063/1.2130720>, doi:10.1063/1.2130720. \_eprint: [https://pubs.aip.org/aip/apl/article-pdf/doi/10.1063/1.2130720/13168422/204104\\_1\\_online.pdf](https://pubs.aip.org/aip/apl/article-pdf/doi/10.1063/1.2130720/13168422/204104_1_online.pdf).
- [18] Jankauskas, A., Mažeika, L., 2011. Wind turbine blade analysis using ultrasonic guided waves. URL: [https://www.ndt.net/article/CompNDT2011/papers/15\\_Jankauskas.pdf](https://www.ndt.net/article/CompNDT2011/papers/15_Jankauskas.pdf).
- [19] Kosova, F., Özkan Altay, Özgür Ünver, H., 2025. Structural health monitoring in aviation: a comprehensive review and future directions for machine learning. *Nondestructive Testing and Evaluation* 40, 1–60. URL: <https://doi.org/10.1080/10589759.2024.2350575>, doi:10.1080/10589759.2024.2350575, arXiv:<https://doi.org/10.1080/10589759.2024.2350575>.
- [20] Kudela, P., Polish Academy of Sciences (PAS), Fiborek, P., Polish Academy of Sciences (PAS), Ostachowicz, W.M., 2024. Wave Propagation for Structural Health Monitoring (WaveProSHM): open software with GUI. *e-Journal of Nondestructive Testing* 29. URL: <https://www.ndt.net/search/docs.php?i=29639>, doi:10.58286/29639.
- [21] Love, A.E.H., 1888. The small free vibrations and deformation of a thin elastic shell. *Philosophical Transactions of the Royal Society of London. A* 179, 491–546. URL: <http://www.jstor.org/stable/90527>.
- [22] Mondaic, . Spectral element modelling suite salvus. URL: <https://www.mondaic.com/solutions#non-destructive-testing>.
- [23] Mustapha, S., Saad, D.M., Fakih, M.A., Yuan, F.G., 2024. Composite sandwich structures: Damage detection and assessment using ultrasonic guided waves, in: *Structural Health Monitoring/management (SHM) in Aerospace Structures*. Elsevier, pp. 55–99. URL: <https://linkinghub.elsevier.com/retrieve/pii/B9780443154768000162>, doi:10.1016/B978-0-443-15476-8.00016-2.
- [24] Olisa, S.C., Khan, M.A., Starr, A., 2021. Review of Current Guided Wave Ultrasonic Testing (GWUT) Limitations and Future Directions. *Sensors* 21, 811. URL: <https://www.mdpi.com/1424-8220/21/3/811>, doi:10.3390/s21030811.
- [25] Ostachowicz, W., Kudela, P., Radzieński, M., 2024. Identification of composite material properties by elastic wave propagation methods, in: *Structural Health Monitoring/management (SHM) in Aerospace Structures*. Elsevier, pp. 389–408. URL: <https://linkinghub.elsevier.com/retrieve/pii/B9780443154768000010>, doi:10.1016/B978-0-443-15476-8.00001-0.
- [26] Park, B., Sohn, H., Malinowski, P., Ostachowicz, W., 2017. Delamination localization in wind turbine blades based on adaptive time-of-flight analysis of noncontact laser ultrasonic signals. *Nondestructive Testing and Evaluation* 32, 1–20. URL: <https://www.tandfonline.com/doi/full/10.1080/10589759.2015.1130828>, doi:10.1080/10589759.2015.1130828.
- [27] Raghavan, A., Cesnik, C.E.S., 2007. Review of Guided-wave Structural Health Monitoring. *The Shock and Vibration Digest* 39, 91–114. URL: <http://svd.sagepub.com/cgi/doi/10.1177/0583102406075428>, doi:10.1177/0583102406075428.
- [28] Thomsen, H.R., Van Manen, D.J., Baettig, S., Brauner, C., Gebraad, L., Boehm, C., 2024. The W-Scan: leveraging guided waves to create digital twins for non-destructive evaluation of composite materials, Brugg-Windisch.

- [29] Tikhonov, A.N., 1963. On the solution of ill-posed problems and the method of regularization. Dokl. Akad. Nauk SSSR 151, 501–504. URL: <https://www.mathnet.ru/eng/dan/v151/i3/p501>. english translation available via MathNet.Ru.
- [30] Wan, L., Ismail, Y., Sheng, Y., Ye, J., Yang, D., 2023. A review on micromechanical modelling of progressive failure in unidirectional fibre-reinforced composites. Composites Part C: Open Access 10, 100348. URL: <https://www.sciencedirect.com/science/article/pii/S266668202300004X>, doi:<https://doi.org/10.1016/j.jcomc.2023.100348>.
- [31] Waqar, M., Memon, A.M., Sabih, M., Alhems, L.M., 2024. Composite pipelines: Analyzing defects and advancements in non-destructive testing techniques. Engineering Failure Analysis 157, 107914. URL: <https://www.sciencedirect.com/science/article/pii/S1350630723008683>, doi:<https://doi.org/10.1016/j.engfailanal.2023.107914>.
- [32] Wilcox, P., Monkhouse, R., Lowe, M., Cawley, P., 1998. The Use of Huygens' Principle to Model the Acoustic Field from Interdigital Lamb Wave Transducers. Springer US, Boston, MA. pp. 915–922. URL: [https://doi.org/10.1007/978-1-4615-5339-7\\_118](https://doi.org/10.1007/978-1-4615-5339-7_118), doi:10.1007/978-1-4615-5339-7\_118.
- [33] Wueest, R., 2025. Github repository to the code, as well as further documentation. <https://github.com/Fiidch/Fully-Vectorized-Linear-Operator-Formulation-for-Inverse-Scattering-Problems>.
- [34] Yawn, K.R., Drake, T.E., Osterkamp, M.A., Chuang, S.Y., Acres, P., Thomas, M., Kaiser, D., Marquardt, C., Filkins, B., Lorraine, P., Martin, K., Miller, J., 1999. Large-Scale Laser Ultrasonic Facility for Aerospace Applications. Springer US, Boston, MA. pp. 387–393. URL: [https://doi.org/10.1007/978-1-4615-4791-4\\_48](https://doi.org/10.1007/978-1-4615-4791-4_48), doi:10.1007/978-1-4615-4791-4\_48.
- [35] Yu, S., Luo, K., Fan, C., Fu, K., Wu, X., Chen, Y., Zhang, X., 2025. Advancing spacecraft safety and longevity: A review of guided waves-based structural health monitoring. Reliability Engineering & System Safety 254, 110586. URL: <https://linkinghub.elsevier.com/retrieve/pii/S0951832024006574>, doi:10.1016/j.ress.2024.110586.